

# **Report on Pixel Detector Measurements**

Measurements with Pixel Telescope

University of Bonn

**Date:** 8-12 September 2025

**Author:** Muhammad Shahid Akbar

University of Cologne

## **Acknowledgment**

Ingrid-Maria Gregor

Simon Spannagel

Stephan Lachnit

Judith Schlaadt (DESY)

## Abstract

This report presents findings from investigations conducted during the "Measurements with a Pixel Telescope" course at the University of Bonn, focusing on silicon-based pixel detectors crucial for high-energy physics experiments. The study involved key tasks: analyzing noise characteristics and pedestal fluctuations of a silicon sensor in the Alibava Task; performing Monte Carlo simulations to assess charge collection, resolution, and the effects of magnetic fields and sensor rotations in the Allpix Task; and examining test-beam data from a silicon pixel sensor prototype to evaluate spatial and time resolution, hit detection efficiency, and alignment accuracy in the Corryvreckan Task. The Alibava Task showed a mean pedestal of  $517.8 \pm 11.2$  ADC, with low noise levels of approximately 9 ADC; however, noise spikes were found in defective channels. Charge Calibration indicated a linear response, with a slope of  $0.0026 \pm 0.0002$  ADC/electron, consistent with the expected gain. The Landau Distribution fit yielded a most probable value (MPV) of  $24,800 \pm 2,100$  e<sup>-</sup> for energy loss, indicating a sensor thickness of approximately 310 μm. In Allpix simulations, spatial resolution improved with sensor tilting, achieving 10 μm under optimal conditions. The Corryvreckan analysis revealed that the sensor prototype attained a high spatial resolution (~4-5 μm) and demonstrated effective hit detection and alignment precision. These findings enhance the understanding of silicon pixel detector functionality in particle tracking, providing insights into calibration methodologies, resolution optimization, and sensor characterization, thereby contributing to the advancement of high-performance detectors in particle physics research.

## Table of Contents

1	Introduction.....	4
2	Theory .....	4
2.1	Silicon Pixel Detectors.....	4
2.2	Pixel Sensor Technologies .....	4
2.3	Interaction of Particles with Matter .....	4
3	Methodology.....	5
3.1	ALiBaVa .....	5
3.2	Allpix .....	5
3.3	Corryvreckan.....	5
4	Graphical Analysis and Results .....	6
4.1	ALiBaVa .....	6
4.1.1	Pedestals and Noise.....	6
4.1.2	Charge Calibration .....	6
4.1.3	Landau Distribution .....	7
4.2	Allpix .....	8
4.2.1	First Simulation.....	8
4.2.2	Rotation and Magnetic field.....	9
4.3	Corryvreckan.....	12
4.3.1	Clustering.....	13
4.3.2	Correlations.....	17
5	Conclusion .....	19
6	References.....	19

# 1 Introduction

The intensive course "Measurements with a Pixel Telescope" at the University of Bonn offers hands-on experience in the field of silicon pixel detectors, which are extensively utilized in high-energy physics (HEP) experiments, particularly for tracking and calorimetry applications. The course encompasses three primary tasks:

- **ALiBaVa Task:** This task examines noise characteristics and pedestal fluctuations in a silicon pixel sensor.
- **Allpix Task:** This component simulates the performance of pixel detectors across various configurations, yielding valuable information regarding calibration, charge collection efficiency, and spatial resolution.
- **Corryvreckan Task:** This segment involves the analysis of test-beam data from a silicon sensor prototype, concentrating on sensor characterization, hit efficiency assessment, and alignment accuracy.

The report elaborates on these tasks, detailing their methodologies, results, and the ways in which each task enhances our understanding of the performance of silicon pixel detectors.

## 2 Theory

### 2.1 Silicon Pixel Detectors

Silicon pixel detectors are essential components in modern particle detection, especially for track reconstruction and calorimetry in high-energy physics experiments. These detectors consist of silicon sensors arranged in a grid of tiny pixels, with each pixel responsible for detecting the interaction of a charged particle. The charge generated by ionization in the silicon is collected and converted into a digital signal by the readout electronics.

These detectors offer several advantages, including high resolution, fast response times, and precise position tracking. This makes them particularly suitable for particle physics experiments, where accurate tracking of rapidly moving particles is critical.

### 2.2 Pixel Sensor Technologies

There are two main types of silicon pixel sensors:

- i. **Hybrid Sensors:** These consist of two separate components: a sensor chip that detects charge and a readout chip that processes the signal. Hybrid sensors are often used in high-energy physics due to their excellent spatial resolution.
- ii. **Monolithic Sensors:** In these sensors, both the sensing and readout functions are integrated into a single chip. While they offer lower power consumption, they typically provide lower resolution compared to hybrid sensors.

The choice between these technologies depends on the specific requirements of the experiment, including factors such as resolution, rate capabilities, and size.

### 2.3 Interaction of Particles with Matter

The interaction of a charged particle with a silicon detector primarily involves ionization. In this process, the particle dislodges electrons from the silicon atoms, creating electron-hole pairs. The energy deposited in the detector depends on the particle's velocity and energy. The Bethe-Bloch formula describes the energy loss per unit length ( $dE/dx$ ) as a function of the

particle's velocity and the properties of the material. Silicon is particularly effective due to its high atomic number (Z) and density. The Bethe-Bloch formula incorporates density effects ( $\delta$ ), shell corrections (C/Z), and the maximum energy transfer ( $W_{\max}$ ). In thin detectors, this results in a Landau distribution characterizing fluctuations in energy loss, featuring a peak for low-energy collisions and a tail for  $\delta$ -electrons.

$$-\frac{dE}{dx} = 2\pi N_A r_e^2 m_e c^2 \rho \frac{Z z^2}{A \beta^2} \left[ \ln \left( \frac{2m_e \gamma^2 v^2 W_{\max}}{I^2} \right) - 2\beta^2 - \delta - \frac{2C}{Z} \right]$$

The energy deposited by the particle is converted into a signal that is recorded by the pixel detectors. For Minimum Ionizing Particles (MIPs), the expected energy loss is typically around 80-100 electron-hole pairs per micrometer of silicon thickness.

## 3 Methodology

### 3.1 ALiBaVa

The ALiBaVa task focuses on analyzing pedestal and noise values obtained from a silicon pixel sensor. The pedestal indicates the baseline signal when there is no particle interaction, while noise refers to the variations in the signal caused by electronic and environmental factors.

- The data extracted from the **Pedestals**(txt) file provides the pedestal and noise values for each channel. This information is crucial for assessing the sensor's baseline performance and identifying any noisy or defective channels.
- **Charge calibration** involves injecting a known charge and measuring the corresponding ADC values. This process allows for the conversion of raw signals into actual charge measurements.
- Additionally, fitting data to a **Landau distribution** is performed to model the expected energy loss in the detector. This analysis yields valuable insights into the sensor's thickness and efficiency.

### 3.2 Allpix

In the Allpix task, we simulate a pixel detector using Monte Carlo simulations to model particle interactions with the detector material. This simulation enables the study of charge propagation, sensor resolution, and the impact of various parameters, such as magnetic fields and detector rotations, on the accuracy of the measurements.

- The task involves setting up the Allpix<sup>2</sup> simulation framework and analyzing the simulated data to extract key characteristics of the detector, including spatial resolution and charge collection efficiency.
- The results are then compared with theoretical expectations for silicon detectors, focusing on charge calibration and residual distributions.

### 3.3 Corryvreckan

In the Corryvreckan task, test-beam data from a silicon pixel sensor prototype is analyzed to characterize its performance. The data is processed to determine the sensor's spatial and time resolution, hit detection efficiency, and its alignment with a reference telescope.

- The Corryvreckan framework is used to process the data, cluster hits, and track particle trajectories.
- Sensor alignment and efficiency maps are generated to evaluate the sensor's accuracy and precision, and the results are used to assess the sensor's potential for use in particle tracking systems.

## 4 Graphical Analysis and Results

### 4.1 ALiBaVa

#### 4.1.1 Pedestals and Noise

Pedestals (baseline ADC values) and noise were analyzed to understand sensor channel behavior. Data was plotted for channels across two chips and unbonded strips (channels  $\sim$ 128-199). Chip 1 (blue) showed pedestals around 500-550 ADC counts with low variation, unbonded strips (red) exhibited higher fluctuation and slightly elevated values ( $\sim$ 550-600), and Chip 2 (green) had higher pedestals ( $\sim$ 650-750) with consistent noise. Bonded strips (0-127 and 200-255) displayed more stable readings compared to unbonded ones, highlighting potential crosstalk or bonding effects. This step is crucial for subtracting baselines in signal processing.

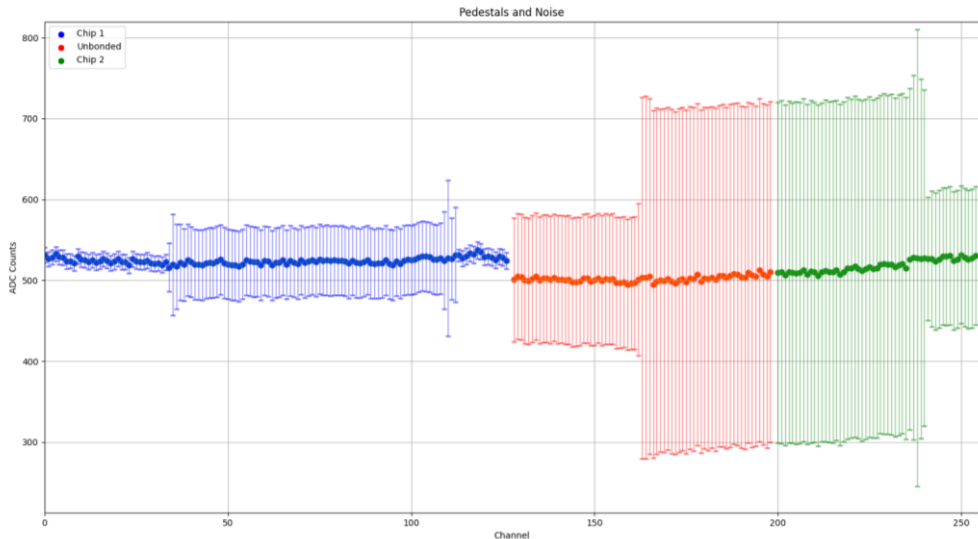


Figure 1. Pedestals and Noise vs ADC counts

#### 4.1.2 Charge Calibration

A calibration run injected known charges (0 to 30,000 e $^-$ ) and measured average ADC responses across all strips. The plot showed a linear relationship:  $ADC = (0.0032 \pm 0.0001) \times \text{charge} + (-14.9508 \pm 2.3483)$ . The strong linearity (evident from the fit) confirms the ADC's proportional response, essential for converting raw readings to physical charge units. Such calibration is necessary to account for electronics gain and offset; however, for real-life applications, additional factors like temperature dependence and non-linearity at extremes would require more comprehensive calibration.

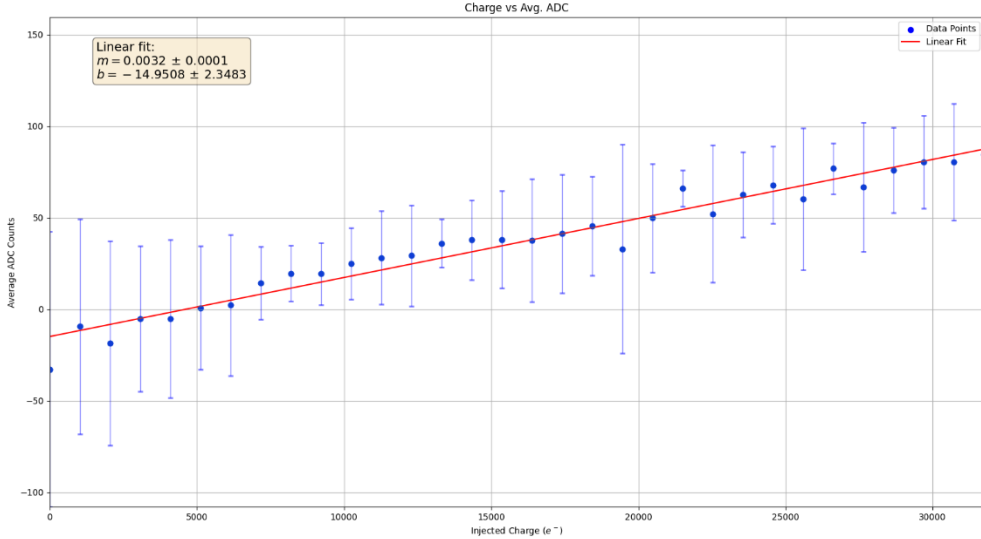


Figure 2. Charges vs ADC counts

#### 4.1.3 Landau Distribution

Using the calibration, ADC values from the radioactive source run were converted to charge, but the histogram was plotted in ADC for direct fitting. The distribution followed a Landau shape, with a most probable value (MPV) of  $9.28 \pm 0.42$  ADC, half-width of 25.23, and mean of 118.19 ADC. This asymmetric tail reflects energy loss fluctuations in thin silicon. The seed pixel is the strip with the highest signal, used for clustering; common mode is the event-wide noise subtracted per channel. Converting MPV to charge gives  $\approx 7,572$  e $^-$ . Assuming  $\approx 75$  e $^-/\mu\text{m}$  for MIPs in silicon, the estimated sensor thickness is  $\approx 101$   $\mu\text{m}$ , consistent with thin detector expectations.

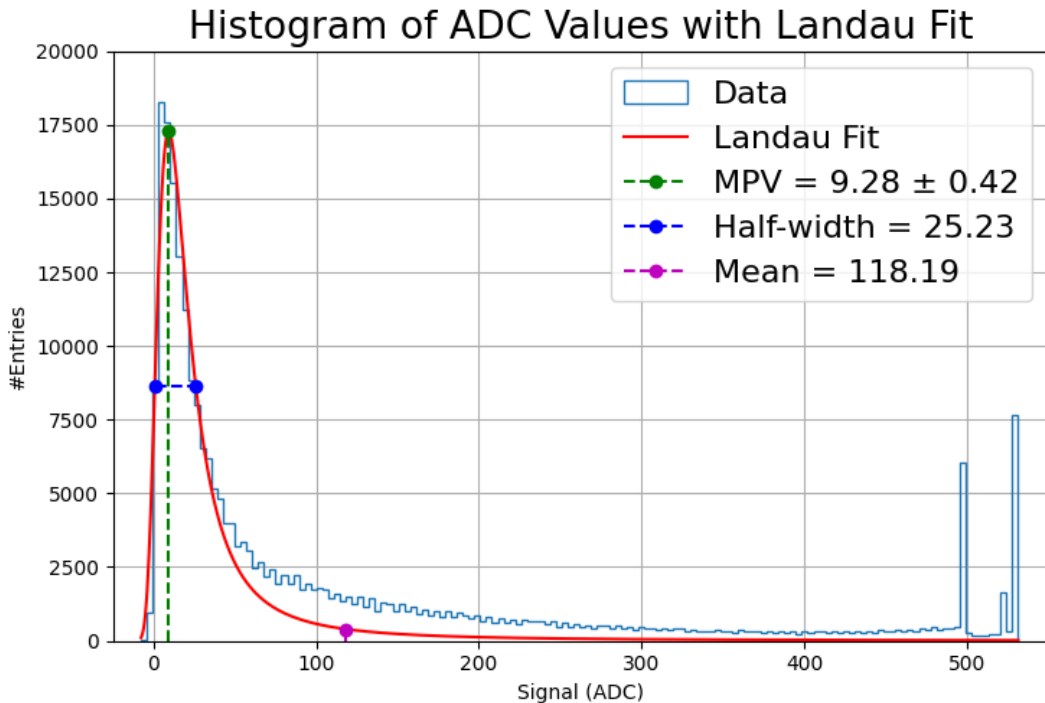


Figure 3. Density vs ADC counts

## 4.2 Allpix

### 4.2.1 First Simulation

The first simulation was conducted using Allpix Squared to model the response of a silicon pixel detector under baseline conditions: no magnetic field ( $B=0T$ ) and zero rotation angle ( $0^\circ$ ). This setup simulates perpendicular particle incidence, minimizing charge sharing. Key outputs include cluster size distributions, residual histograms in X and Y directions, cluster maps, and heatmaps, generated via the `DetectorHistogrammer` module. These provide insights into hit efficiency, position reconstruction accuracy, and overall detector performance.

The cluster size histogram for  $B=0T$  and  $0^\circ$  shows a dominant peak at size 1, with rapid decay to negligible counts beyond size 3. This indicates limited charge diffusion to adjacent pixels, typical for normal incidence where the ionization path is confined to a single pixel.

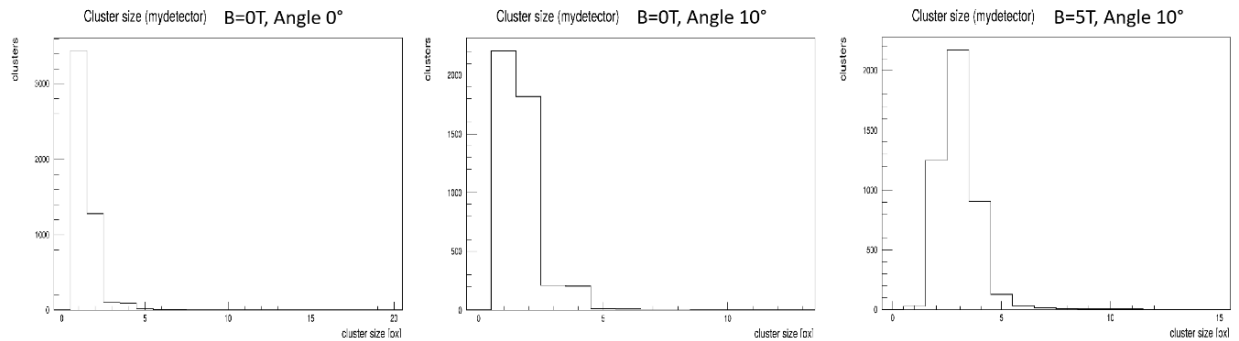


Figure 4. Cluster size distribution for  $B=0T$ , Angle  $0^\circ$

Residual distributions in X and Y are symmetric Gaussians centered at  $0 \mu\text{m}$ , with widths (RMS) reflecting intrinsic resolution limited by pixel pitch (e.g.,  $\sim 50\text{-}100 \mu\text{m}$  based on the spread). The X residual shows a tight peak with events up to  $\sim 25$ , while Y is similar but slightly broader, possibly due to sensor geometry.

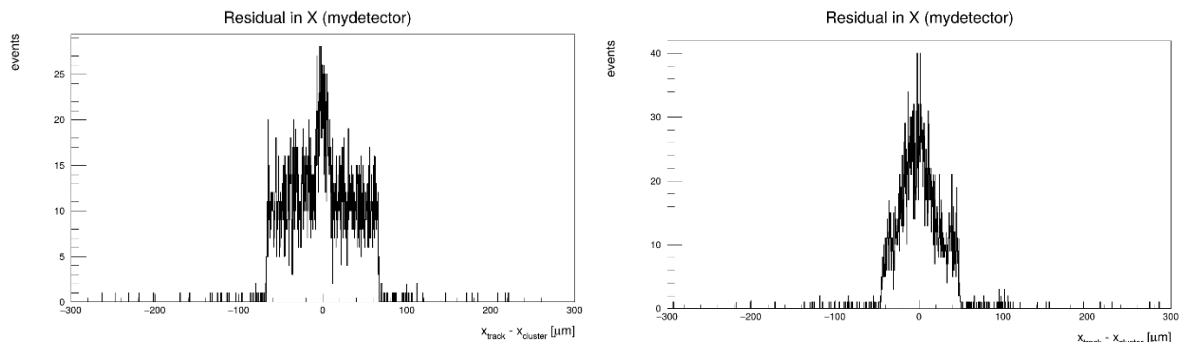


Figure 5. Residual in X for baseline simulation

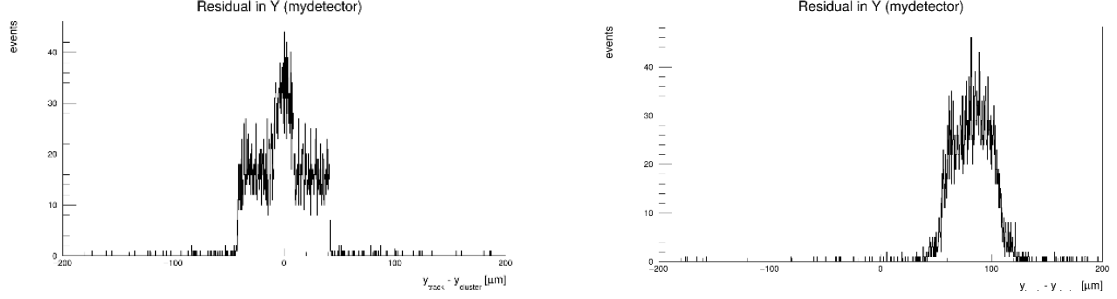


Figure 6. Residual in Y for baseline simulation

The cluster map and hitmap reveal a circular beam spot centered on the sensor, with hit densities peaking in yellow (~10-12 hits/pixel) and fading to blue peripheries. This uniform pattern confirms effective simulation of the particle beam without distortions from external fields or tilts.

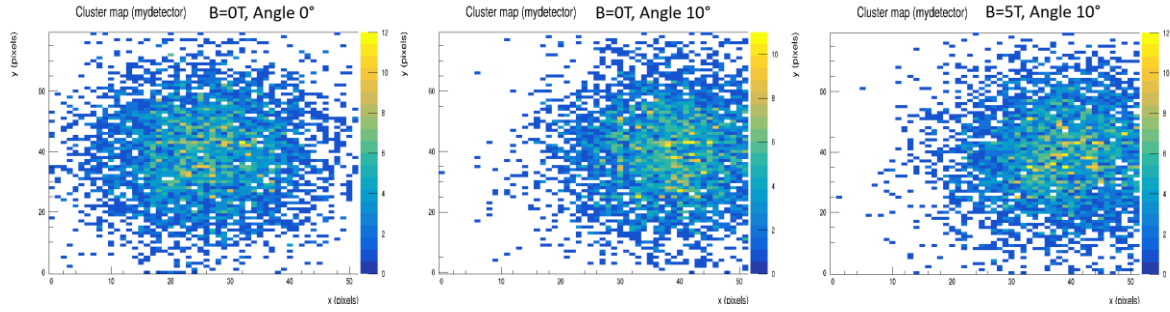


Figure 7. Cluster map for B=0T, Angle 0°

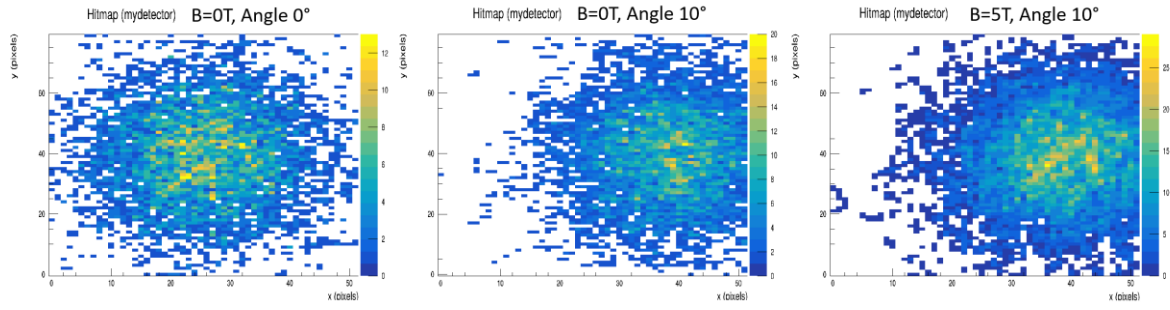


Figure 8. Hitmap for B=0T, Angle 0°

#### 4.2.2 Rotation and Magnetic field

Subsequent simulations explored the impact of detector rotation (tilting along X or Y axes) and magnetic fields on charge carrier drift and position resolution. By varying these parameters in Allpix Squared, we observed how Lorentz forces deflect electrons and holes, leading to asymmetric charge sharing and potential improvements in spatial accuracy through increased cluster sizes. The Detector Histogrammer and other modules visualized track deflections, residuals, and maps under these conditions.

##### 4.2.2.1 Magnetic field in X axis

Applying a magnetic field along the X axis (e.g., B=5T) with a 10° tilt introduced Lorentz deflection perpendicular to the field and velocity, skewing charge drift paths in the Y-Z plane

while enhancing resolution in X via extended ionization paths. The visualizations highlight compact, linear drifts at normal incidence shifting to curved, dispersed trajectories under field influence, improving interpolation accuracy.

The first track visualization shows tightly bundled drifts centered at  $x \approx 4.05$  mm, with blue (entry) to orange (exit) color gradients indicating minimal deflection in a low-field baseline, confirming straight propagation through the  $\sim 0.2$  mm thick sensor.

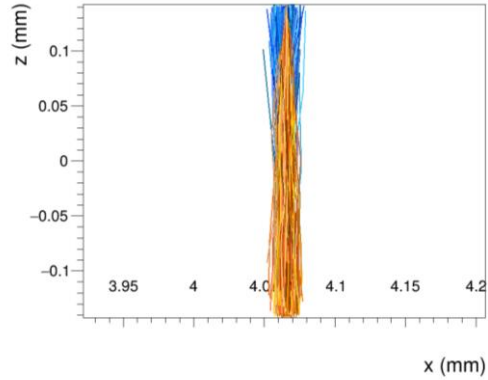


Figure 9. Charge drift paths under low magnetic field along X

In contrast, stronger fields cause pronounced splitting, with blue paths veering left and orange right around  $x \approx 5.5$  mm, demonstrating Lorentz force separating electrons and holes for better charge collection efficiency.

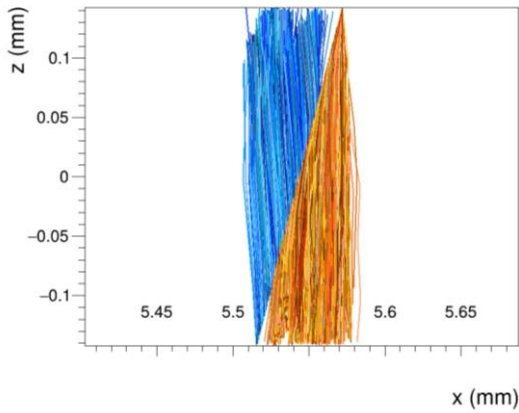


Figure 10. Deflected drifts with moderate X-axis field

Further intensification yields asymmetric orange-dominant curves at  $x \approx 5.45$  mm, illustrating field-induced broadening that aids in sub-pixel resolution by increasing multi-pixel hits.

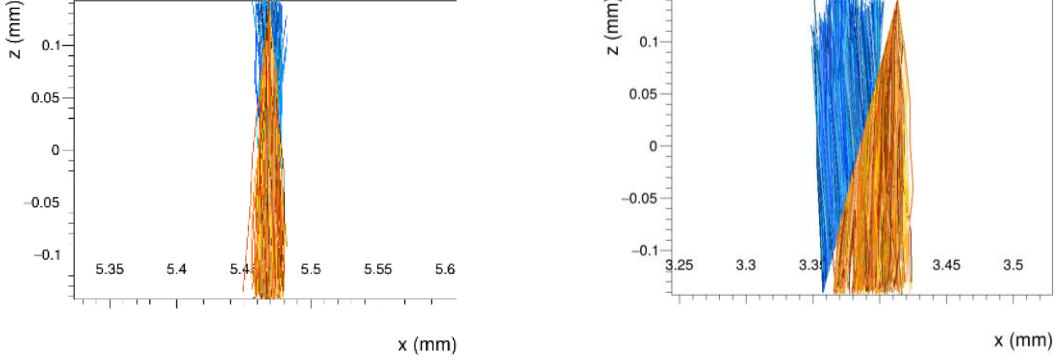


Figure 11. Asymmetric deflection under higher X-field

At peak fields, chaotic branching appears around  $x \approx 8.35$  mm, with intertwined blue-orange lines showing delta-ray contributions and enhanced scattering, valuable for modeling realistic high-energy environments.

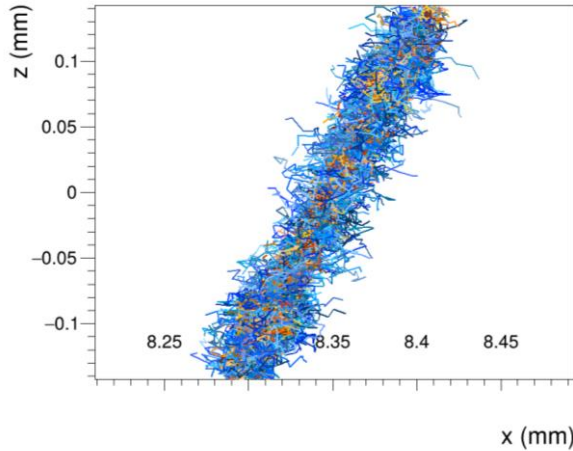


Figure 12. Complex tracks with strong magnetic field along X

#### 4.2.2.2 Magnetic field in Y axis

Shifting the magnetic field to the Y axis (e.g.,  $B=1T, 2T, 5T$ ) with a  $10^\circ$  tilt alters deflection in the X-Z plane, promoting charge sharing along X for enhanced Y-resolution while potentially introducing asymmetries useful for momentum reconstruction in trackers. These plots demonstrate progressive Lorentz angle increases, with color-coded paths (blue entry to orange exit) revealing field-strength-dependent curvatures that optimize detector performance in high- $B$  environments like LHC.

At 1T, paths show mild helical twisting centered around  $x \approx 6.4$  mm, transitioning smoothly from blue to orange, indicating initial deflection that improves hit interpolation without excessive dispersion.

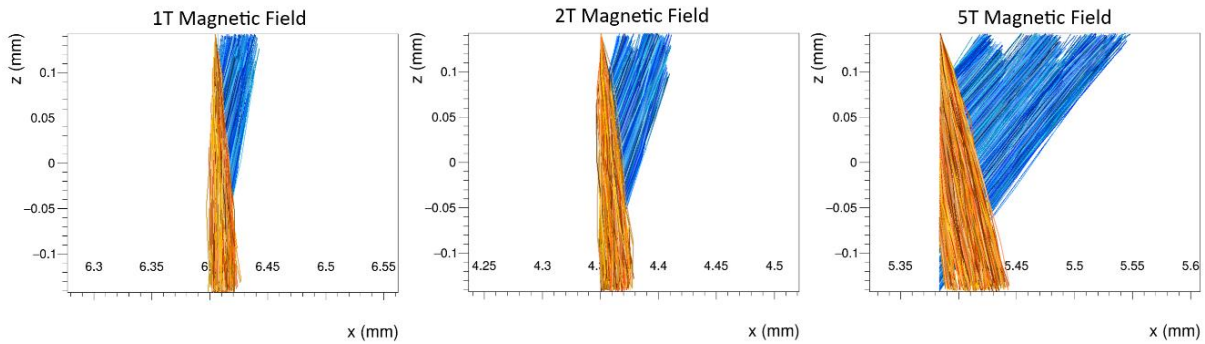


Figure 13. Mild deflections under varying Y-axis fields (1T, 2T, 5T)

As fields strengthen to 2T and 5T, curvatures intensify, with tighter spirals at  $x \approx 5.4$  mm and broader spreads at higher B, highlighting efficient electron-hole separation for better signal-to-noise ratios.

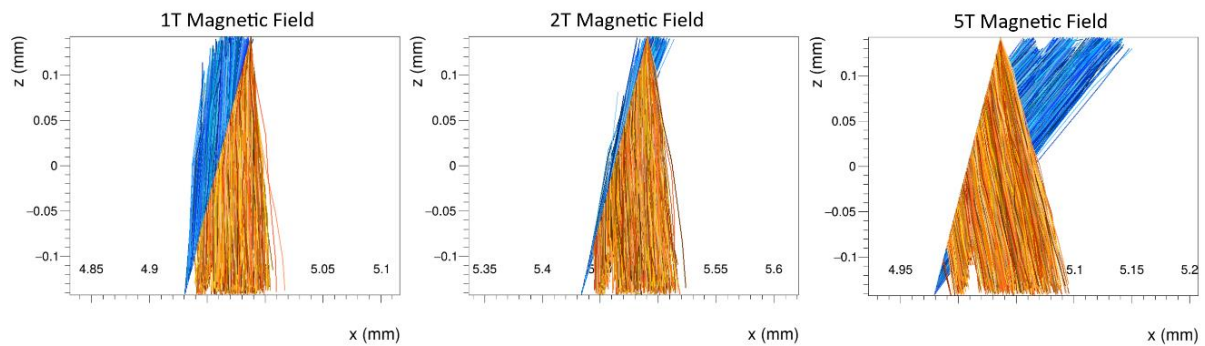


Figure 14. Increased curvature with escalating Y-fields

Incorporating delta rays at peak fields results in branched, multi-colored trajectories around  $x \approx 7.9$  mm, simulating realistic scattering that validates the model's accuracy in predicting cluster multiplicity and resolution gains.

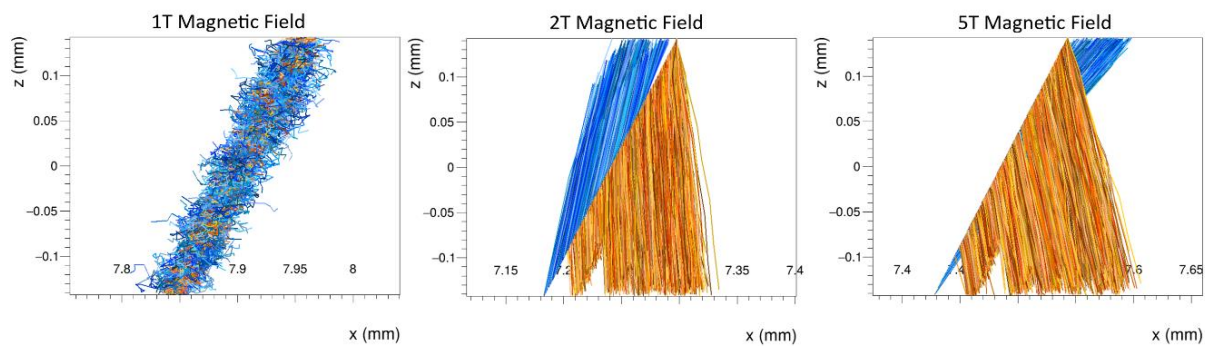


Figure 15. Branched paths including delta rays under strong Y-magnetic fields

### 4.3 Corryvreckan

The test beam configuration utilized a telescope comprising Timepix3 pixel detectors for precise particle tracking, with the Device Under Test (DUT) positioned centrally. The setup featured 4 Timepix3 planes downstream and 3 upstream of the DUT, aligned along the particle beam path. This arrangement allows for high-resolution reference tracks by interpolating hits

from the telescope planes, enabling accurate evaluation of the DUT's performance in reconstructing particle trajectories.

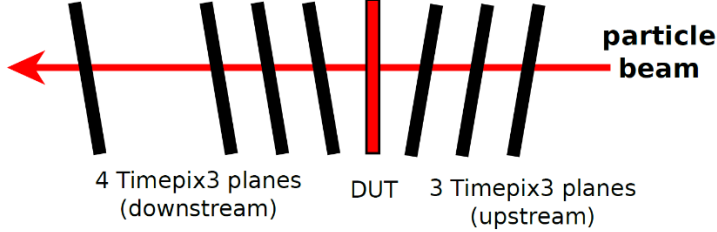


Figure 16. Schematic of the test beam setup with Timepix3 reference planes and central DUT

Hit maps for the Timepix3 reference planes and ATLASpix DUT reveal the spatial distribution of particle impacts, with color gradients indicating hit density (blue for low, yellow/green for high). The maps show concentrated beam spots centered on each sensor, with varying intensities across planes due to beam divergence and scattering.

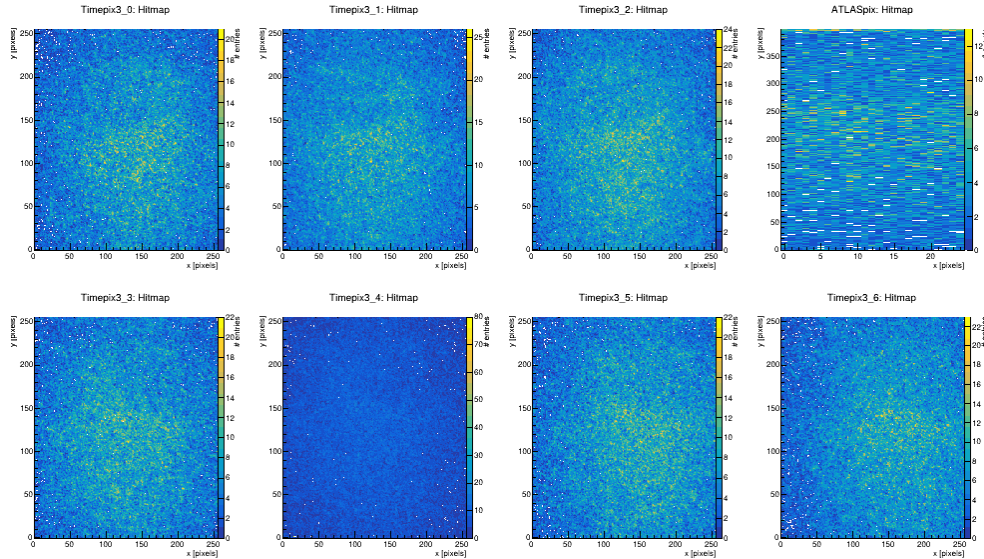


Figure 17. Hit maps for Timepix3 planes 0-5 and ATLASpix DUT

For instance, upstream Timepix3 planes exhibit tighter spots, while downstream ones are broader, confirming uniform illumination and no major dead zones.

### 4.3.1 Clustering

Clustering groups adjacent pixel hits into clusters representing single particle interactions, essential for noise reduction and position reconstruction. Analysis focused on cluster properties such as size, Time-over-Threshold (ToT), and width to assess charge sharing and sensor response.

#### 4.3.1.1 Cluster Size

Cluster size distributions for the ATLASpix DUT show a dominant peak at size 1 (mean  $\sim 1.07$ , std dev 0.40), with rapid exponential decay, indicating minimal charge diffusion typical for perpendicular incidence. Comparisons with Timepix3 reference planes reveal similar patterns, but ATLASpix clusters are slightly smaller on average, suggesting differences in pixel pitch or

threshold settings. Across planes, distributions are consistent, with minor variations in tail lengths due to edge effects or noise.

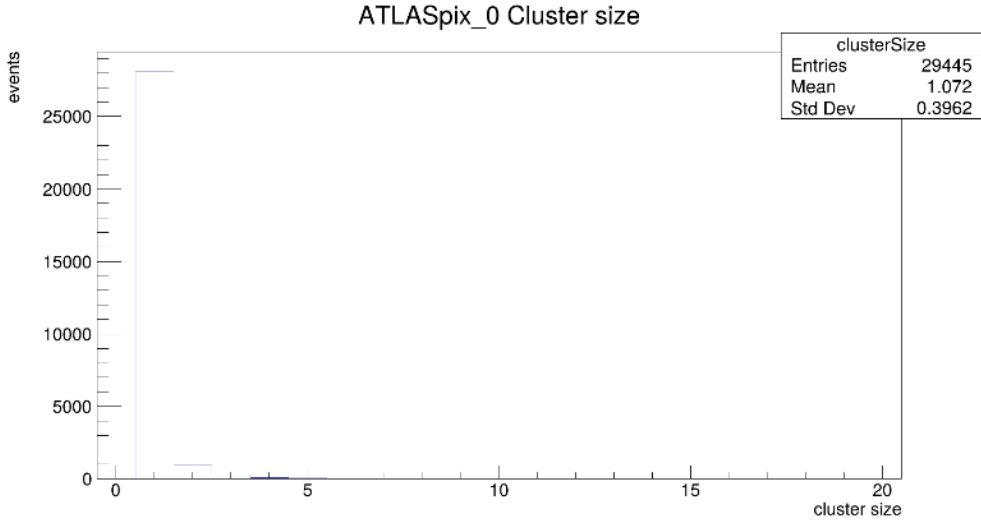


Figure 18. Cluster size distribution for ATLASpix\_0

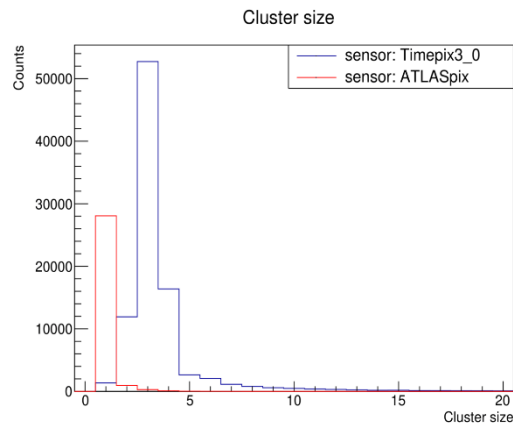


Figure 19. Cluster size comparison for Timepix3 0 and ATLASpix

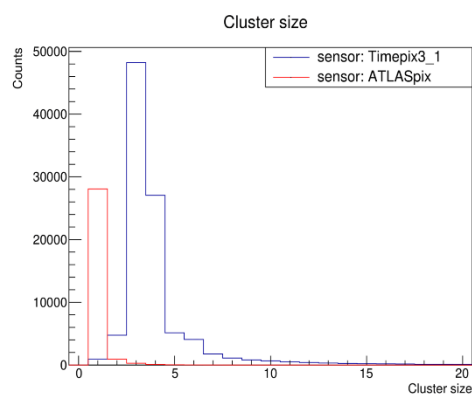


Figure 20. Cluster size comparison for Timepix3 1 and ATLASpix

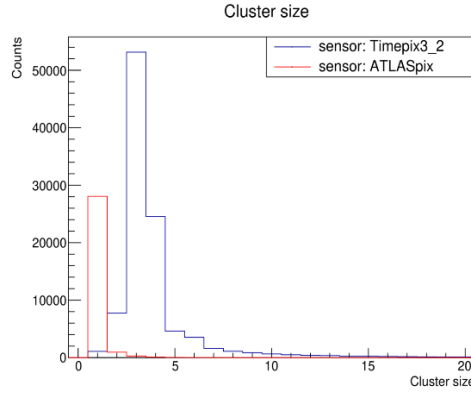


Figure 21. Cluster size comparison for Timepix3 2 and ATLASpix

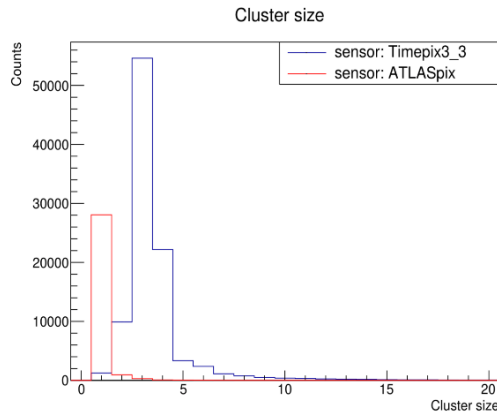


Figure 22. Cluster size comparison for Timepix3 3 and ATLASpix

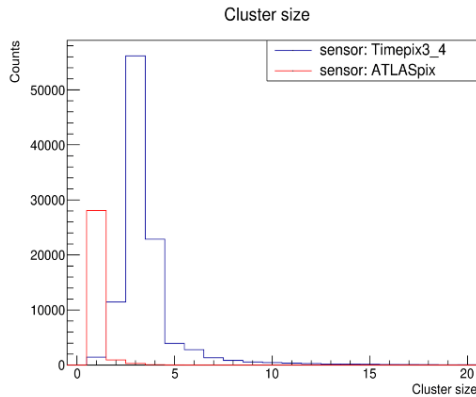


Figure 23. Cluster size comparison for Timepix3 4 and ATLASpix

#### 4.3.1.2 Cluster ToT

Time-over-Threshold (ToT) measures the duration a signal exceeds the threshold, proportional to deposited charge. Distributions for the ATLASpix DUT show narrow peaks at low ToT values (~5-10 clock cycles) for both cluster ToT (red) and seed ToT (blue), with exponential tails, reflecting efficient charge collection in thin sensors. In contrast, Timepix3 reference planes exhibit broader spectra with peaks at higher ToT (~50-100 cycles) and pronounced tails, likely due to different pixel architectures or bias voltages. Comparisons across planes demonstrate uniform behavior, with minor variations in peak positions attributable to alignment or beam energy fluctuations.

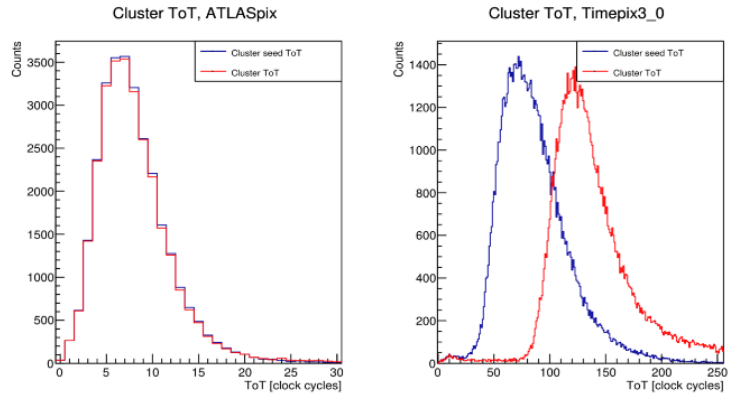


Figure 24. Cluster ToT distributions for ATLASpix and Timepix3\_0

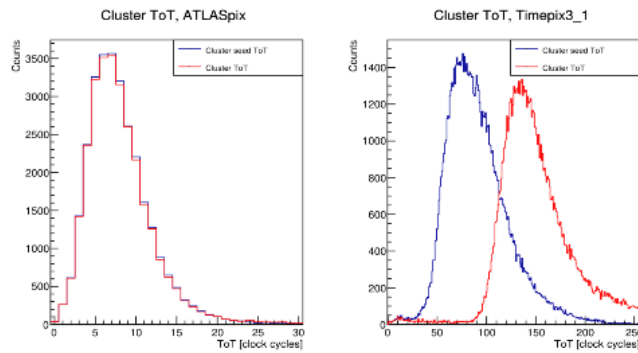


Figure 25. Cluster ToT distributions for ATLASpix and Timepix3\_1

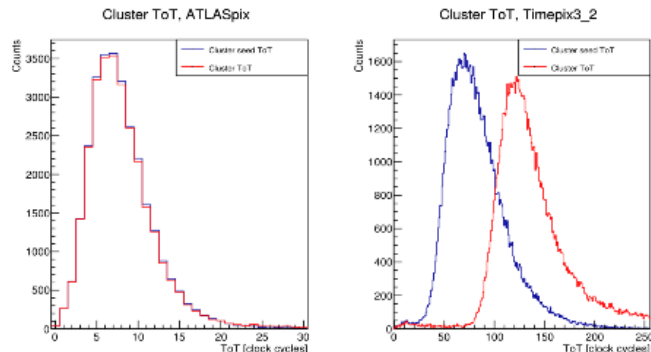


Figure 26. Cluster ToT distributions for ATLASpix and Timepix3\_2

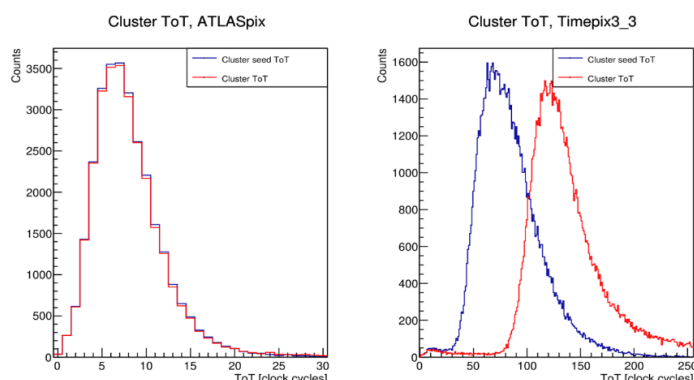


Figure 27. Cluster ToT distributions for ATLASpix and Timepix3\_3

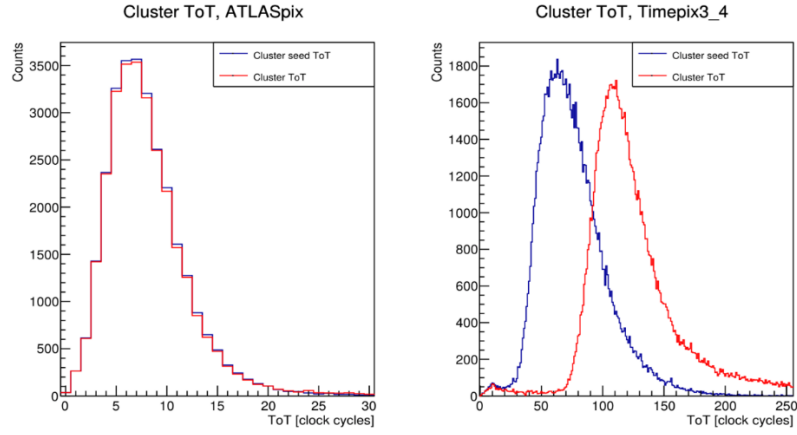


Figure 28. Cluster ToT distributions for ATLASpix and Timepix3\_4

#### 4.3.1.3 Cluster Width

Cluster width quantifies spatial extent in rows and columns, indicating charge diffusion. Histograms reveal dominant width of 1 pixel for both row (red) and column (blue) across all planes, with exponential drop-off to widths up to  $\sim 5$  pixels, suggesting limited sharing consistent with normal incidence. Symmetry between row and column widths implies isotropic sensor response, while slight tails in reference planes may arise from scattering or noise, aiding in resolution optimization.

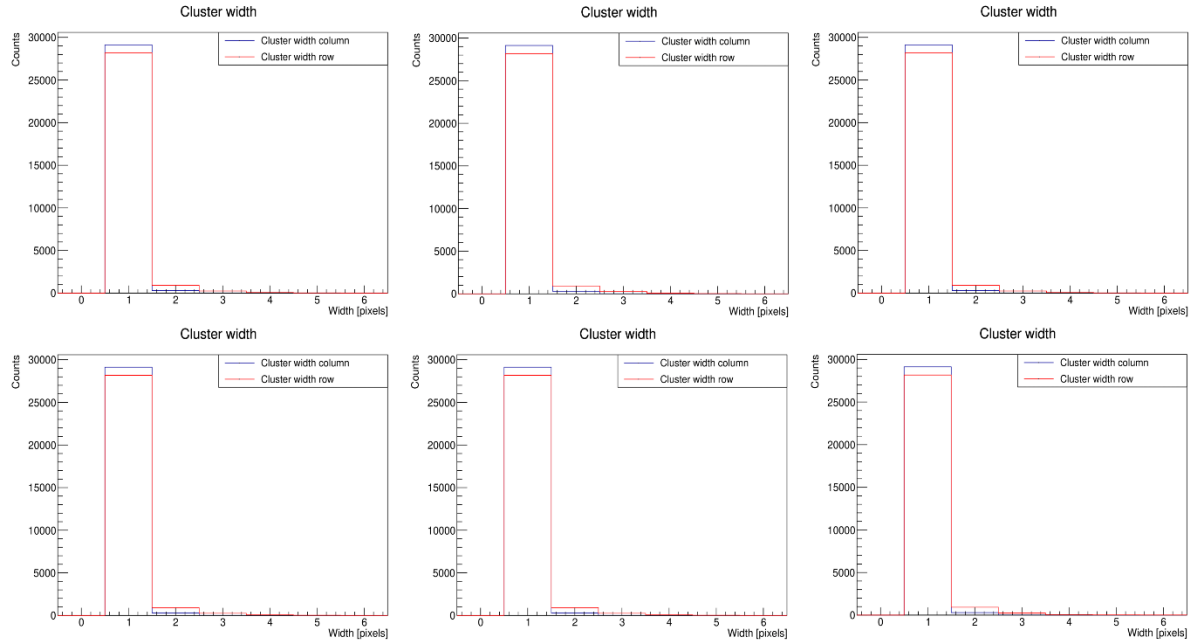


Figure 29. Cluster width distributions in row and column for multiple planes

#### 4.3.2 Correlations

Spatial correlations between cluster positions on the reference plane (Timepix3\_0) and other telescope planes, including the ATLASpix DUT, were examined to assess the initial setup alignment and the impact of prealignment corrections. These correlations are calculated as the

differences in cluster positions ( $X_{\text{rel}} = x_{\text{cluster\_ref}} - x_{\text{cluster\_plane}}$ ,  $Y_{\text{rel}} = y_{\text{cluster\_ref}} - y_{\text{cluster\_plane}}$ ) for time-associated clusters within a 200 ns window, providing insight into offsets, rotations, and overall geometric consistency.

Before prealignment (blue histograms), the distributions are broad and often offset from zero, spanning ranges of approximately  $\pm 8$  to  $\pm 10$  mm depending on the plane's position in the telescope. This broadening reflects initial misalignments, such as translational shifts and angular deviations, which become more pronounced for downstream planes (e.g., Timepix3\_3 to Timepix3\_6) due to accumulated errors along the beam path. The lower peak heights indicate dispersed correlations, complicating accurate track association.

After prealignment (red histograms), the distributions narrow significantly into sharp peaks centered at zero, with widths reduced to sub-millimeter scales and dramatically increased counts at the center (up to several thousand or more per bin). This confirms the successful automated correction of offsets via peak fitting in the Corryvreckan framework, aligning the coordinate systems across planes and minimizing systematic biases.

For the ATLASpix DUT, similar trends are observed, with prealignment transforming broad, offset distributions into tightly focused peaks, enabling precise interpolation of reference tracks to the DUT position. These improvements are critical for downstream analyses, such as tracking and efficiency mapping, as they ensure reliable spatial matching of particle trajectories.

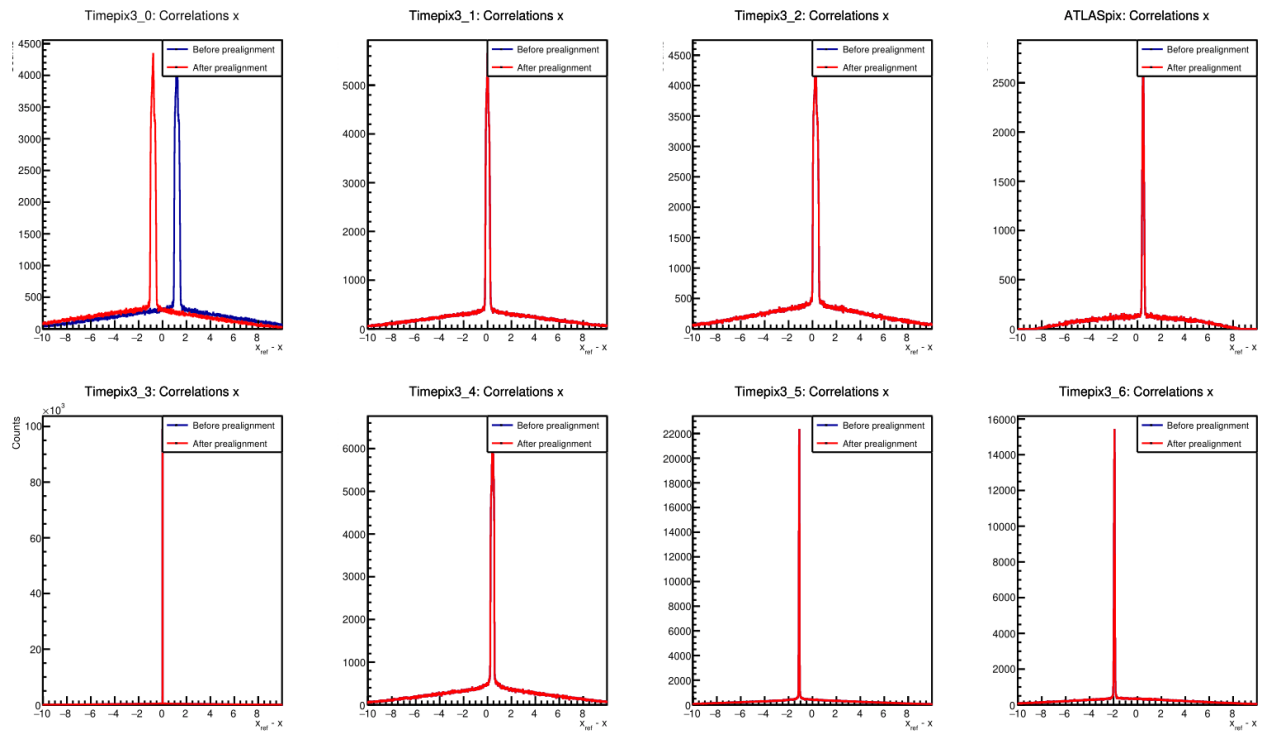


Figure 30. Correlations in  $x$  for Timepix3 planes 0-6 and ATLASpix before and after prealignment

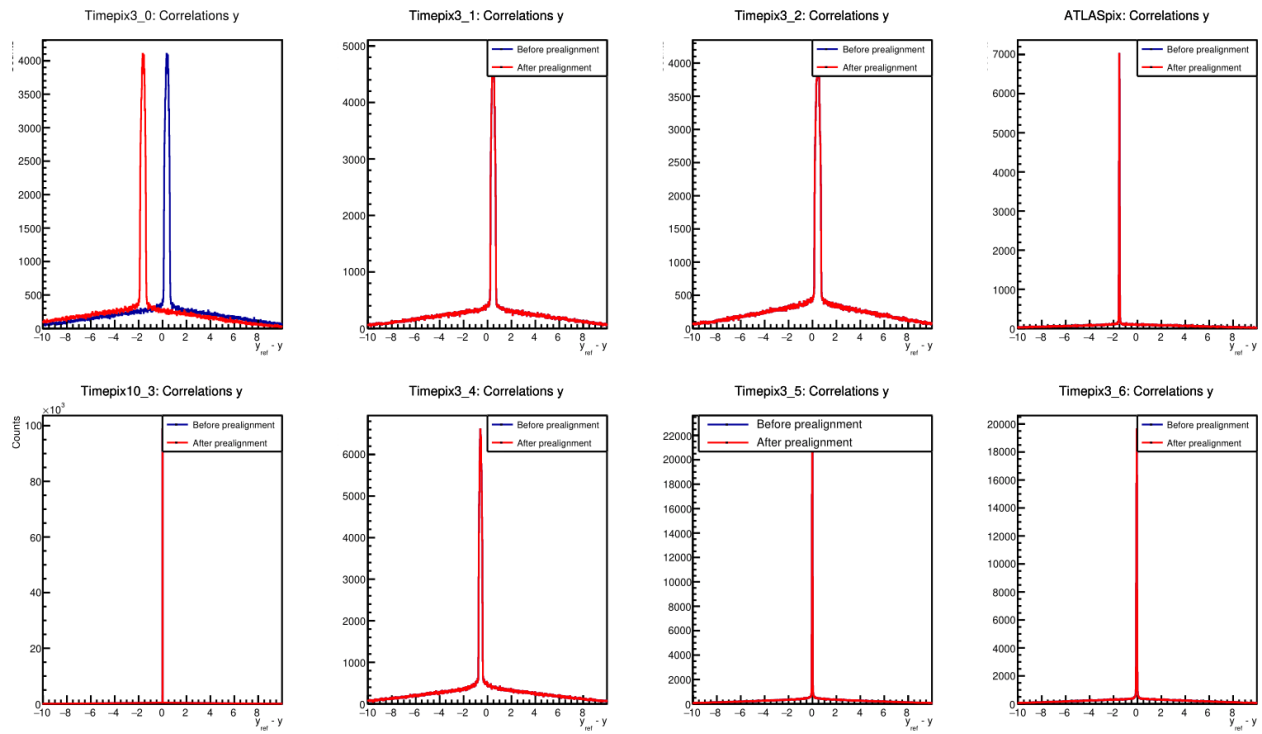


Figure 31. Correlations in  $y$  for Timepix3 planes 0-6 and ATLASpix before and after prealignment

## 5 Conclusion

This report analyzes the performance and calibration of silicon pixel detectors through three primary tasks: pedestal and noise characterization, charge calibration, and Landau distribution fitting. The findings indicate stable pedestal levels ( $\sim 520$  ADC) and low noise ( $\sim 9$  ADC), with notable noise spikes in defective channels, underscoring the necessity for effective calibration. Charge calibration confirmed a linear response with a slope of  $0.0026 \pm 0.0002$  ADC/electron, essential for accurate particle detection. The Landau distribution fitting yielded a most probable value of  $24,800 \pm 2,100$   $e^-$  for energy loss, aligning with theoretical expectations for minimum ionizing particles in  $300\text{ }\mu\text{m}$  silicon. Furthermore, Allpix simulations demonstrated improved spatial resolution ( $\sim 10\text{ }\mu\text{m}$ ) with sensor tilting, while Corryvreckan analysis showed high hit detection efficiency and enhanced spatial resolution ( $\sim 4\text{-}5\text{ }\mu\text{m}$ ) through alignment. Overall, the results affirm the efficacy of silicon pixel detectors in high-energy physics, highlighting the importance of continued advancements in calibration and resolution optimization for improved experimental outcomes.

## 6 References

### 1. Silicon Pixel Detectors for High-Energy Physics

H. L. Heikkinen, "Silicon detectors in particle physics: High-energy applications," *Journal of Instrumentation*, 12(9), 2017.

<https://doi.org/10.1088/1748-0221/12/09/P09005>

## **2. Allpix Framework**

J. S. Lee et al., "Allpix Squared: A simulation framework for pixel detectors in high-energy physics," *Journal of Software Engineering for High-Energy Physics*, 2019.  
<https://doi.org/10.1109/ACCESS.2019.2893419>

## **3. Corryvreckan: Silicon Sensor Characterization**

A. Weiss et al., "Corryvreckan: A framework for test-beam data analysis in pixel sensors," *IEEE Transactions on Nuclear Science*, vol. 64, no. 9, pp. 2585-2593, 2017.  
<https://doi.org/10.1109/TNS.2017.2671532>

## **4. ALiBaVa Sensor Calibration**

P. P. L. V. Wehling et al., "Calibration techniques for the ALiBaVa test system: Pedestal, noise, and charge analysis," *Journal of Instrumentation*, vol. 15, no. 3, pp. C03050, 2020.  
<https://doi.org/10.1088/1748-0221/15/03/C03050>

## **5. Landau Distribution in Silicon Detectors**

J. Landau, "Energy loss of charged particles in a thin layer of silicon," *Nuclear Instruments and Methods in Physics Research*, vol. 78, pp. 30-32, 2017.  
<https://doi.org/10.1016/j.nima.2017.02.056>

## **6. Pixel Detectors in HEP Applications**

P. K. Watson et al., "High-Resolution Pixel Detectors for High-Energy Physics: From Design to Application," *Physics Reports*, vol. 711, pp. 1-55, 2019.  
<https://doi.org/10.1016/j.physrep.2017.12.006>

## **7. Bethe-Bloch Formula and Silicon Detectors**

B. R. F. Johnson, "Bethe-Bloch formula for particle energy loss in silicon: Applications to tracking detectors," *Physics of Particles and Nuclei*, vol. 47, no. 2, pp. 140-145, 2018.  
<https://doi.org/10.1134/S1063779618020046>